High-Order Finite-Volume Transport on the Cubed Sphere: Comparison between 1D and 2D Reconstruction Schemes

KIRAN K. KATTA

University of Texas at El Paso, El Paso, Texas

RAMACHANDRAN D. NAIR

National Center for Atmospheric Research, Boulder, Colorado

VINOD KUMAR

University of Texas at El Paso, El Paso, Texas

ABSTRACT

This paper presents two finite-volume (FV) schemes for solving linear transport problems on the cubed-sphere grid system. The schemes are based on the central-upwind finite-volume (CUFV) method, which is a class of Godunov-type method for solving hyperbolic conservation laws, and combines the attractive features of the classical upwind and central FV methods. One of the CUFV schemes is based on a dimension-by-dimension approach and employs a fifth-order one-dimensional (1D) Weighted Essentially Nonoscillatory (WENO5) reconstruction method. The other scheme employs a fully two-dimensional (2D) fourth-order accurate reconstruction method. The cubed-sphere grid system imposes several computational challenges due to its patched-domain topology and nonorthogonal curvilinear grid structure. A high-order 1D interpolation procedure combining cubic and quadratic interpolations is developed for the FV schemes to handle the discontinuous edges of the cubed-sphere grid. The WENO5 scheme is compared against the fourth-order Kurganov–Levy (KL) scheme formulated in the CUFV framework. The performance of the schemes is compared using several benchmark problems such as the solid-body rotation and deformational-flow tests, and empirical convergence rates are reported. In addition, a bound-preserving filter combined with an optional positivity-preserving filter is tested for nonsmooth problems. The filtering techniques considered are local, inexpensive, and effective. A fourth-order strong stability preserving explicit Runge–Kutta time-stepping scheme is used for integration. The results show that schemes are competitive to other published FV schemes in the same category.

1. Introduction

Because of inherent conservative properties and geometric flexibility, finite-volume-based (FV) discretization techniques are becoming popular for new generation global atmospheric models. The cubed-sphere grid system (Sadourny 1972; Ronchi et al. 1996) provides quasi-uniform grid structures (control volumes) for atmospheric modeling, which is also an ideal system for FV horizontal discretization. The cubed-sphere grid system is free of polar singularities and the control volumes (grid cells) are logically rectangular leading to efficient parallel implementation (Yang and Cai 2011). In recent years, several new models have been developed that exploit computationally attractive features associated with the FV discretization and cubed-sphere geometry (Putman and Lin 2007; Cheruvu et al. 2007; Chen and Xiao 2008; Ullrich et al. 2010).

The cubed-sphere consists of six identical spherical surfaces defined by local coordinate systems that are discontinuous at the edges and corners. Therefore, a major difficulty in adopting the cubed-sphere geometry arises from the "handling" of the edges, where a special treatment is required. As the order of the discretization increases, the issue becomes more complex.

Corresponding author address: Vinod Kumar, The University of Texas at El Paso, 500 W. University Ave., Engineering Building, Room A-219, El Paso, TX 79902.
E-mail: vkumar@utep.edu

To predict the cell averages at the new time level, FV methods require a reconstruction procedure for fluxes at the cell edges from the known cell averages. This involves a computational halo region (stencil) encompassing several grid cells. A fully two-dimensional (2D) FV approach requires ghost cell creation at the cubed-sphere corner. However, a dimension-by-dimension approach employing two 1D reconstructions along the coordinate directions greatly simplifies the problem. A major concern with the dimension-by-dimension approach, the resulting FV scheme suffers from reduction in formal order of accuracy, and this issue might be more severe in nonorthogonal curvilinear grid such as cubed-sphere grid. This motivates us to compare the performance of 1D and 2D reconstruction high-order FV schemes for a variety of benchmark tests on the cubed sphere.

We consider a high-order FV discretization based on the so-called central-upwind finite-volume (CUFV) method introduced by Kurganov and Levy (2000) and Kurganov and Petrova (2001). The CUFV scheme is a semidiscretized method combining the attractive properties of the classical upwind and central FV methods. Its features include easy A-grid (unstaggered) implementation with simple Riemann solvers (numerical flux). Because of its semidiscretized (spatially discretized) formulation, the time integration can be performed by explicit multistage Runge–Kutta (RK) solvers resulting in high-order temporal accuracy and increased Courant–Friedrichs–Lewy (CFL) stability limit. A recent application of CUFV method for ocean and atmospheric modeling can be found in (Adamy et al. 2010; Nair and Katta 2013). For the present work, we consider two high-order spatial discretizations (reconstructions). The dimension-by-dimension version of the FV scheme is based on the fifth-order Weighted Essentially Nonoscillatory (WENO5) method (Liu et al. 1994; Shu 1997). For multidimensional application, high-order 2D WENO schemes are computationally prohibitive and rarely used for practical purpose. Therefore, we consider a fully 2D fourth-order FV discretization as given in Kurganov and Liu (2012). Our main focus here is to evaluate the dimension-by-dimension WENO5 reconstructions in a CUFV framework for linear transport problem on a nonorthogonal curvilinear cubed-sphere grid. The performance of WENO5 scheme is compared with a CUFV scheme based on 2D reconstructions as well as various other high-order FV schemes developed on the cubed sphere. In addition, we discuss strictly positivity-preserving filters for both CUFV schemes.

The paper is organized as follows. Section 2 describes CUFV schemes based on 1D and 2D reconstructions and its implementation on cubed sphere. In section 3, time integration schemes and positivity-preserving filters are discussed. Numerical experiments are described in section 4, followed by summary and conclusions in section 5.

2. CUFV formulation

a. 2D linear transport on cubed sphere

We consider the flux-form transport equation in (x^1, x^2) space, without a source term as follows:

$$\frac{\partial U}{\partial t} + \nabla \cdot \mathbf{F}(U) = 0, \quad \text{in} \quad D \times (0, T], \quad \forall \quad (x^1, x^2) \in D, \tag{1}$$

where $U = U(x^1, x^2, t)$ is conservative quantity, with the initial condition $U_0 = U(t = 0)$, and T is the final time. In (1), gradient operator $\nabla = (\partial/\partial x^1, \partial/\partial x^2)$ and the flux function $\mathbf{F} = (F_1, F_2)$. In the case of a cubed sphere, the computational domain D spans six identical nonoverlapping subdomains (faces Ω^k) of the cubed-sphere surface; (x^1, x^2) are the central angles such that $(x^1, x^2) \in [-\pi/4, \pi/4]$, subjected to equiangular central projection (Rančić et al. 1996; Nair et al. 2005). Each subdomain Ω^k is partitioned into $N_c \times N_c$ nonoverlapping rectangular cells $\Omega_{i,j}$, where $i, j = 1, 2, \ldots, N_c$, so that $\Omega_{ij} = [(x^1 \in (x^1_{i-1/2}, x^1_{i+1/2}), x^2 \in (x^2_{j-1/2}, x^2_{j+1/2})]$. Thus, the total number of cells on the cubed sphere are $6 \times N_c \times N_c$. In Fig. 1a a cubed sphere tiled with FV grid cells is shown, where $N_c = 10$ and cell centers are indicated by dots. The width of each cell is $\Delta x^1_i = (x^1_{i+1/2} - x^1_{i-1/2})$ and $\Delta x^2_j = (x^2_{j+1/2} - x^2_{j-1/2})$, in x^1 and x^2 directions, respectively.

The advection equation in the curvilinear coordinates on a sphere without the source term is equivalent to the following:

$$\frac{\partial U}{\partial t} + \frac{1}{\sqrt{g}} \frac{\partial}{\partial x^1} [u^1 \sqrt{g} U] + \frac{1}{\sqrt{g}} \frac{\partial}{\partial x^2} [u^2 \sqrt{g} U] = 0. \tag{2}$$

The equation can be rearranged similar to (1) in the following flux form (Levy et al. 2007):

$$\frac{\partial}{\partial t} [\phi] + \frac{\partial}{\partial x^1} [F_1(\phi)] + \frac{\partial}{\partial x^2} [F_2(\phi)] = 0, \tag{3}$$

where $\phi = \sqrt{g} U$, and fluxes $F_1(\phi) = u^1 \phi$, $F_2(\phi) = u^2 \phi$, with contravariant velocity vectors (u^1, u^2). Note that the metric term $\sqrt{g}$ has an explicit analytical form in terms of (x^1, x^2); details of the transformations and metric tensor are given in Nair et al. (2005) and Levy et al. (2007), and will not be discussed herein. Thus, the solution procedure for (3) in (x^1, x^2) space is similar to that for the 2D Cartesian case.

b. CUFV schemes

A large class of FV methods for solving hyperbolic conservation laws are based on high-order extensions of
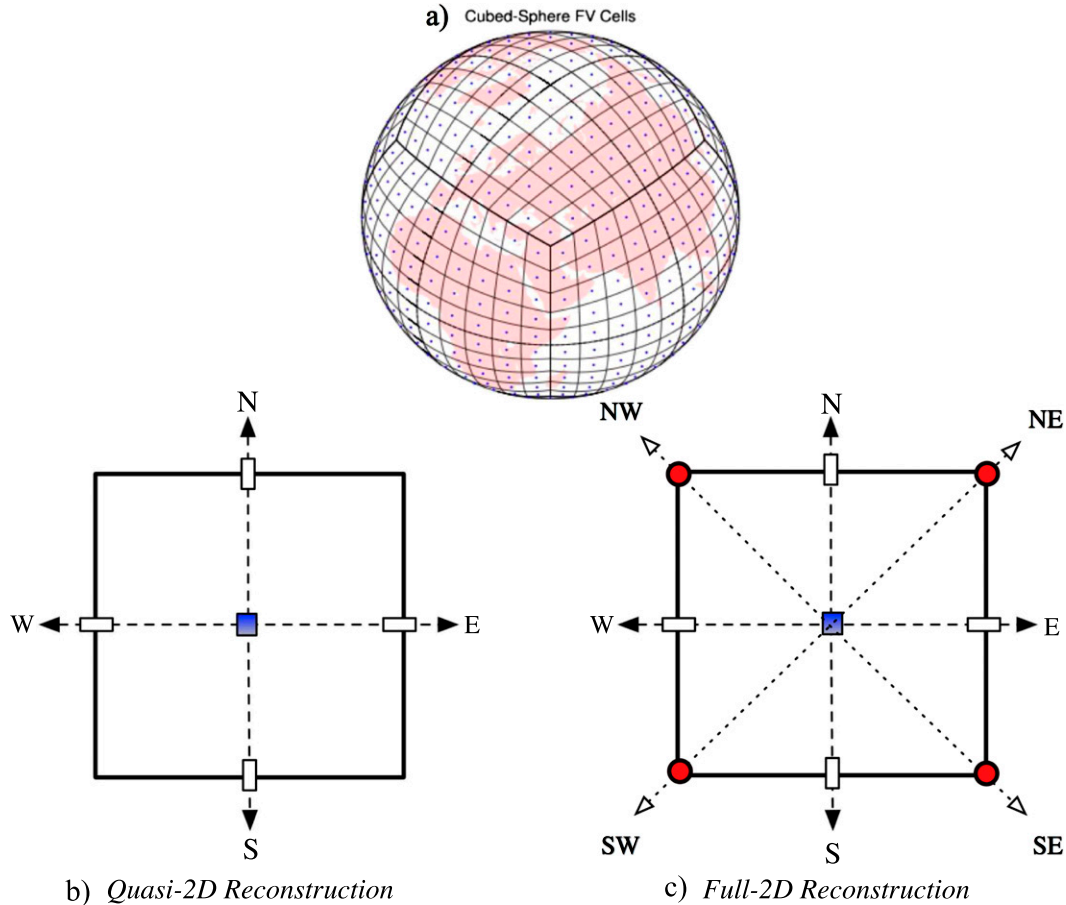
FIG. 1. Schematic showing a cubed sphere (a) with rectangular FV cells, total $6 \times N_c^2$ cells ($N_c = 10$), which span the entire surface. The flux points along the FV cell walls required for the (b) dimension-by-dimension and (c) fully 2D cases.

the Godunov scheme (Godunov 1959), collectively known as the Godunov-type schemes (Toro 1999). These schemes essentially have three basic steps in the solution process: reconstruction, evolution, and projection. In reconstruction step, piecewise polynomials are reconstructed over the grid cells spanning the domain from the known cell averages (piecewise constant data) at the previous time level (van Leer 1974; Colella and Woodward 1984). In evolution step, the piecewise polynomials are advanced in time, following the underlying conservation law. At the final projection step, new cell averages are computed on each cell by projecting the evolved polynomials onto cell averages. Such Godunov-type schemes are broadly classified into *upwind* and *central* schemes. The CUFV combines these two methods resulting in a class of semidiscrete (continuous in time) scheme, which are relatively simple and are easy to implement in various applications. Its novel features include high-order accuracy, use of simple numerical flux, and can be implemented in a nonstaggered grid system when used

for a system of equations. These make CUFV computationally attractive for complex domain such as the cubed-sphere considered here. Detailed discussion of CUFV schemes including mathematical derivations, properties, and various practical applications can be found in a series of papers (see Kurganov and Levy 2000; Kurganov and Petrova 2001; Kurganov and Liu 2012).

The semidiscrete formulation corresponding to (1) can be written as follows:

$$\frac{d\overline{U}_{ij}}{dt} = \frac{-1}{\Delta x_i^1 \Delta x_j^2} \left[\sum_{e=1}^{4} \int_{\Gamma_e} \mathbf{H}_e \cdot \mathbf{n}_e \right], \qquad (4)$$

where $\overline{U}_{ij}$ is the cell average, $\mathbf{H}_e \cdot \mathbf{n}_e$ is the numerical flux defined at the cell walls (interfaces), and $\mathbf{n}_e$ is the unit outward-drawn normal vector from the cell boundary Γ_e. The *average* quantity $\overline{U}_{ij}$, defined over an FV cell Ω_{ij}, is computed by solving the ordinary differential equation (ODE) (4) in time. The order of spatial accuracy and computational efficiency of the FV scheme depends

on the polynomial representation for $\overline{U}_{ij}$ and accuracy of the flux integrals.

Reconstruction functions are piecewise polynomials $P_{ij}^n(x^1, x^2) \approx U_{ij}(x^1, x^2, t^n)|_{\Omega_{ij}}$, representing the subgrid-scale distribution at a time $t = t^n$. They are subjected to the following conservation constraint:

$$\overline{U}_{ij}^n = \frac{1}{\Delta x_i^1 \Delta x_j^2} \int_{x_{j-1/2}^2}^{x_{j+1/2}^2} \int_{x_{i-1/2}^1}^{x_{i+1/2}^1} P_{ij}^n(x^1, x^2)\, dx^1\, dx^2, \quad (5)$$

where $\overline{U}_{ij}^n$ is the cell average at time $t = t^n$. There are several ways to represent $P_{ij}^n(x^1, x^2)$ and formulate reconstruction procedure. The flux values are computed using P_{ij}^n along the boundaries as required in (4). For example, on the east wall of the cell Ω_{ij} (i.e., the edge $x_{i+1/2,j}^1$), we get contributions for $U_{i+1/2,j}$ from the left and right edges of the cell walls. They are usually denoted by $U_{i+1/2,j}^-$ and $U_{i+1/2,j}^+$, respectively. The flux at the point is defined by $H_{i+1/2,j}(U_{i+1/2,j}^-, U_{i+1/2,j}^+)$ and computed by the following formula (Kurganov and Petrova 2001):

$$H_{i+1/2,j}(t) = \frac{F_1[U_{i+1/2,j}^+(t)] + F_1[U_{i+1/2,j}^-(t)]}{2}$$
$$- \frac{a_{i+1/2,j}^1(t)}{2}[U_{i+1/2,j}^+(t) - U_{i+1/2,j}^-(t)], \quad (6)$$

where $a_{i+1/2,j}^1(t)$ is the maximum *local speed* (absolute value of the flux Jacobian $\partial F_1/\partial U$) in the x^1 direction. In linear advection case, the flux formula reduces to the local Lax–Friedrichs (Rusanov) flux as given in (6). For reconstruction functions P_{ij}^n, first we consider a dimension-by-dimension procedure followed by a fully 2D approach as follows.

1) DIMENSION-BY-DIMENSION FIFTH-ORDER WENO RECONSTRUCTIONS

The dimension-by-dimension case combines two sweeps of 1D polynomial functions along the coordinate direction and is subject to the conservation constraint (5). The WENO schemes are known to be robust for solving conservation laws. A comprehensive review for WENO scheme is given in Shu (1997). One can rigorously derive a fifth-order accurate fully 2D WENO scheme using a 5×5 stencil. Unfortunately, resulting scheme is computationally prohibitive and not particularly suitable for the cubed-sphere grid. Therefore, we consider CUFV scheme based on WENO reconstruction method, where a fifth-order accurate 1D reconstruction is used in each coordinate direction, hereafter referred to as WENO5. The WENO5 is one of the most widely used schemes in its class for various applications. Recently, Norman et al. (2011) and Blossey and Durran (2008) used WENO5 for atmospheric modeling; Byron and Levy (2006) applied a
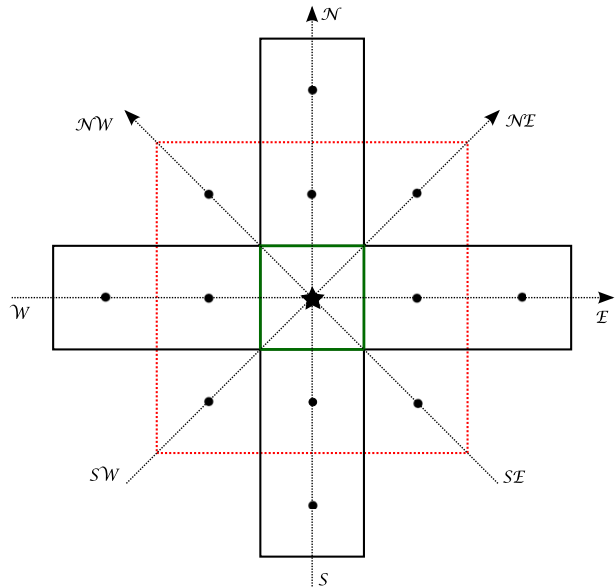

FIG. 2. Schematic of the 2D stencil required for KL scheme where 13 cells are used for reconstructing the fluxes along the cell boundaries (green lines) on the central cell. Black boxes indicate the two 1D stencils for WENO5 scheme, along the west–east and south–north directions, excluding the corner cells. A total of nine cells are required for WENO5 reconstructions.

central WENO5 scheme for a system of conservation laws.

In Fig. 2, a 2D stencil used for the WENO5 is schematically shown with cell centers in the west–east and south–north directions. Flux evaluation for the WENO5 scheme is required only at four cell walls as indicated in Fig. 1b, making the computational procedure relatively simple. A typical WENO reconstruction process involves a main computational stencil and several substencils within. The basic idea of the WENO method is to use a convex combination of reconstructions from all the stencils and employ nonlinear weights to achieve highest possible order of accuracy in smooth regions. The WENO scheme uses a convex combination of nonlinear weights w_k from each stencil, which depends on the local smoothness of the solution, and results in a nonoscillatory solution. The smoothness indicators β_k, which are a measure of the smoothness of the solution, are computed for each stencil. A smaller value of β_k indicates a smoother function. The WENO5 uses a five cell-wide stencil including the cell in question located at the center, where a family of 1D polynomials $P^k(x)$ are employed for reconstruction (Shu 1997). We briefly outline the reconstruction procedure as follows.

The point value required for flux evaluation can be computed using reconstruction functions. For example, at the east wall $U_{i+1/2} = R_{i+1/2}$, where $R_{i+1/2}$ is the

WENO5 reconstruction function at the cell interface $x_{i+1/2}$, and is defined as

$$R_{i+1/2} = \sum_{k=0}^{r-1} w_k P_{i+1/2}^k, \quad \text{where} \quad P_{i+1/2}^k = \sum_{j=0}^{r-1} c_{kj} \overline{U}_{i-k+j},$$
$$k = 0, \ldots, r-1,$$
(7)

where $r = 3$ and the constant coefficients c_{kj} are as given in Liu et al. (1994). The nonlinear weights are defined as follows:

$$w_k = \alpha_k \Big/ \sum_{s=0}^{r-1} \alpha_s, \quad \alpha_k = \frac{c_k}{(\epsilon + \beta_k)^2}, \quad k = 0, \ldots, r-1,$$

where $c_0 = 3/10, c_1 = 3/5,$ and $c_2 = 1/10$, ϵ is small positive number to avoid division by zero, and the smoothness indicator β_k is defined by

$$\beta_0 = \frac{13}{12}(\overline{U}_i - 2\overline{U}_{i+1} + \overline{U}_{i+2})^2 + \frac{1}{4}(3\overline{U}_i - 4\overline{U}_{i+1} + \overline{U}_{i+2})^2,$$

$$\beta_1 = \frac{13}{12}(\overline{U}_{i-1} - 2\overline{U}_i + \overline{U}_{i+1})^2 + \frac{1}{4}(\overline{U}_{i-1} - \overline{U}_{i+1})^2,$$

$$\beta_2 = \frac{13}{12}(\overline{U}_{i-2} - 2\overline{U}_{i-1} + \overline{U}_i)^2 + \frac{1}{4}(\overline{U}_{i-2} - 4\overline{U}_{i-1} + 3\overline{U}_i)^2.$$

The values $U_{i+1/2}^\pm$ at the interfaces are evaluated from the reconstruction functions, followed by computations of the east and west fluxes $H_{i\pm1/2,j}$ using (6). Extending this procedure in x^2 direction yields the fluxes at the north and south walls $H_{i,j\pm1/2}$. Thus, using the WENO5 scheme in a dimension-by-dimension manner (Shu 1997; Kurganov and Petrova 2001) the fluxes at four points (as shown in Fig. 1b) can be computed. Now the 2D semidiscrete scheme in (4) takes the following form:

$$\frac{d}{dt}\overline{U}_{ij}(t) = -\frac{H_{i+1/2,j}(t) - H_{i-1/2,j}(t)}{\Delta x^1}$$
$$-\frac{H_{i,j+1/2}(t) - H_{i,j-1/2}(t)}{\Delta x^2},$$
(8)

which can be solved by a high-order RK ODE solver. Although the dimension-by-dimension approach is relatively easy to implement on the cubed sphere, formal order of accuracy of the resulting scheme may be limited to second order. This is due to the fact that the cross-derivative terms $(\partial U/\partial x^1 \partial x^2)$ are ignored in the polynomial reconstruction.

2) FULLY 2D RECONSTRUCTIONS

We consider the fourth-order fully 2D reconstruction functions used by Kurganov and Liu (2012) combined with the simple equation (6), the resulting CUFV scheme is hereafter referred to as the Kurganov–Levy (KL) scheme. For a FV cell Ω_{ij} in (x, y) Cartesian plane, the reconstruction function is given by

$$P_{ij}(x, y) = a_{0,0} + a_{1,0}(x - x_i) + a_{0,1}(y - y_j) + a_{1,1}(x - x_i)(y - y_j) + a_{2,0}(x - x_i)^2$$
$$+ a_{0,2}(y - y_j)^2 + a_{0,3}(x - x_i)^3 + a_{3,0}(y - y_j)^3 + a_{2,1}(x - x_i)^2(y - y_j)$$
$$+ a_{1,2}(x - x_i)(y - y_j)^2 + a_{4,0}(x - x_i)^4 + a_{2,2}(x - x_i)^2(y - y_j)^2 + a_{0,4}(y - y_j)^4,$$
(9)

where the 13 coefficients $a_{m,n}, 0 \le (m + n) \le 4$, are functions of the partial derivatives (resulting from a Taylor series expansion) $\partial^{m+n}P(x, y)/\partial^m x \partial^n y$, and subject to the conservation constraint (5). Details of the derivation can be found in Kurganov and Liu (2012), however, we provide the coefficients needed for flux computations in appendix A. Note that CUFV scheme using 2D reconstructions (9) requires a computational stencil as shown in Fig. 2.

For a fully 2D scheme, three flux points are located along each cell wall as shown in Fig. 1c. The line integrals along the cell walls are evaluated using three-point Simpson's rule. Here we only show the evaluation for the east wall of Ω_{ij}, and the flux evaluation for the

other walls follow the same pattern. The formula is given as

$$\int_{\Gamma_{\text{East}}} H \cdot \mathbf{n} \approx H_{i+1/2,j}$$
$$= \frac{\Delta x^2}{6}[\hat{H}_{i+1/2,j-1/2} + 4\hat{H}_{i+1/2,j} + \hat{H}_{i+1/2,j+1/2}],$$
(10)

where $\hat{H}_{i+1/2,j+1/2}$ indicates a point-flux evaluation using (6) at the northeast corner, and $H_{i+1/2,j}$ is the net flux at the east wall. Using letter symbols as indicated in Fig. 2, {east (E), west (W), north (N), south (S), southeast (SE), southwest (SW), northeast (NE), northwest (NW)}instead of subscripts $(_{i\pm1/2,j\pm1/2}$, etc.), the flux $H_{i+1/2,j}$ in

(10) can be written as follows (Kurganov and Petrova 2001):

$$H_{i+1/2,j} = \frac{1}{12} \{ F(U_{i+1,j}^{NW}) + F(U_{ij}^{NE}) + 4[F(U_{i+1,j}^{W}) + F(U_{ij}^{E})]$$
$$+ F(U_{i+1,j}^{SW}) + F(U_{ij}^{SE}) - a_{i+1/2,j}^{1} \times [U_{i+1,j}^{NW} - U_{ij}^{NE}$$
$$+ 4(U_{i+1,j}^{W} - U_{ij}^{E}) + U_{i+1,j}^{SW} - U_{ij}^{SE}]\},$$

$$(11)$$

where $a_{i+1/2,j}^{1}$ is the maximum local speed in the x^1 direction. See appendix A for details of flux computations in (11). Using symmetry the fluxes as required in (8), $H_{i-1/2,j}$ and $H_{i,j\pm1/2}$ can be computed.

3) TREATMENT AT THE CUBED-SPHERE EDGES

High-order FV schemes require a wider computational stencil involving several cells. Because of the coordinate discontinuity at the edges of the cubed-sphere face, creation of such stencils is a challenging task for the cubed-sphere grid system. Each face of the cubed sphere has logically rectangular cells, however, by the virtue of equiangular (central) projection this further simplifies (i.e., in the computational domain $\Delta x^1 = \Delta x^2$). For the CUFV scheme considered herein, we employ the computational stencil as seen in Fig. 2, which requires two grid cells on both sides along the coordinate directions for WENO5 (total nine cells), and four additional corner cells (ghost cells, colored in red) in the case of fully 2D reconstructions. On the surface of the cubed-sphere the cell centers (where cell averages are computed) lie along great-circle arcs. We adopt a strategy described in Ronchi et al. (1996), Yang et al. (2010), and Rossmanith (2006), where the grid lines are extended to both edges along the great-circle arcs beyond the usual range $[-\pi/4, \pi/4]$, and perform high-order 1D interpolations. For subdomain extensions, we also exploit a property of the central projection by which the extended points on the overlap regions lie along great-circle arcs. In our case the grid lines need to be further extended by two grid cells (ghost cells) at the edges, which are located on the neighboring panels (see Fig. 3). However, each horizontally extended point (say in the x^1 direction) is straddled by grid points from the adjoining panel along a great-circle arc, but in the vertical (x^2) direction.

To illustrate the 1D interpolation process, we consider two lateral adjoining panels as shown in Fig. 3, where the cell centers are marked as red and blue points, with known spherical coordinates. Let θ_k, $k = 1, 2, \ldots, N$ be the latitudes of cell centers on the right panel (blue points) and located next to the edge line in the x^2 direction. These points serve as source points for 1D interpolation along the great-circle arc, and are marked
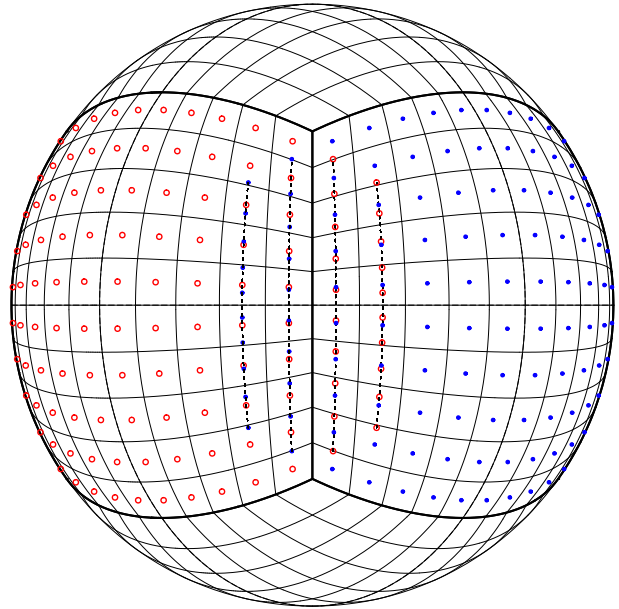

FIG. 3. Horizontal extensions of the cubed-sphere grid points at the edges to form halo regions (cells) required for the CUFV computational stencils. For any two adjoining panels, the extended grid points are exactly located along a great-circle arc joining the grid points from the other panel in the vertical direction, which are shown as dashed lines. 1D interpolations are performed along these lines using the cell averages at regular grid points (source points) to find the cell averages for the extended grid points (target points).

as a *vertical* dotted line in Fig. 3. The target points are positioned at the cell centers of the ghost cells, which are extended on the halo zone. Let the latitudes of target points be θ_k', $k = 1, 2, \ldots, N$, which are located along the same dotted line and denoted by red circles (Fig. 3), in such a way that $\theta_1', \ldots, \theta_N' \in [\theta_1, \theta_N]$. Since the source and target points lie along the same great-circle arc (analogous to a straight line in 2D Cartesian geometry), a *natural* and easy option for finding the values at the target points is by employing 1D high-order interpolations.

We use the cubic-Lagrange interpolation along the dotted lines to compute cell averages at the target points (on halo cells) $\theta_2', \theta_3', \ldots, \theta_{N-1}'$. The values at the corner (halo) point, say at θ_1', can be computed by a quadratic interpolation using the known values at source points θ_1, θ_2, and θ_3; similarly, the cell average at θ_N' can be quadratically interpolated. The cell-average values at the second layer of halo cells required for WENO5 and KL schemes can be computed in a similar manner. Using the symmetry of the cubed-sphere grid system, the source and target coordinates (θ_k, θ_k', $\ldots$) can be reused for any cubed-sphere edges, and the implementation of this procedure is straightforward for the dimension-by-dimension schemes. The combination of cubic and quadratic 1D interpolation avoids using information from the third panel,

and reduces error. Also we found that 1D high-order (quintic) interpolation, which uses information from the third panel, can deteriorate the convergence rate. A fully 2D scheme requires an additional ghost-cell value for the reconstruction at the corner cell (see Fig. 2), which can be interpolated quadratically from the neighboring cell averages. Note that a drawback of this 1D approach may be the use of quadratic interpolation (a lower-order operation) at the corner cell, and computation of ghost-cell values for KL scheme. This may have some adverse effect on the global convergence rate.

Handling of the cubed-sphere edges for fully 2D scheme can be performed in a more sophisticated way for better accuracy, but at a higher computational cost. The multimoment FV scheme by Chen and Xiao (2008) identifies one layer of the target cells on the halo zone as described above. To find the ghost-cell values, a 2D interpolation is performed using the readily available local moments. This method seems to be very accurate but only suitable for multimoment FV schemes. Ullrich et al. (2010) proposed novel high-order FV schemes on the cubed-sphere, where the ghost-cell averages are obtained by using the Gauss quadrature over the target cell, which involves sampling the values at the quadrature points by the local reconstruction polynomials. However, for simplicity we do not employ this method for the KL scheme, rather we use the 1D approach described above. Using the common 1D interpolation procedure for both the WENO5 and KL schemes facilitates a closer comparison.

3. Time integrations and positivity filters

a. Time integration scheme: SSP-RK (5,4)

After the spatial discretization with FV schemes, the continuous equation (3) reduces to a semidiscretized ODE (8), which can be represented in the following general form:

$$\frac{d}{dt}\overline{U}(t) = L(\overline{U}) \text{ in } (0, T],\qquad(12)$$

where L denotes the spatial discretization resulting from CUFV scheme. There are a wide variety of time integrators available to solve the ODE (12). However, we only consider the explicit RK time integration method.

A new class of optimal high-order strong stability preserving (SSP) and low-storage SSP RK schemes with stage $(s) >$ order (p), have been proposed by Spiteri and Ruuth (2002). These schemes are more efficient than the known schemes with $s = p$, due to the increase in the allowable time step, which more than compensates the added computational cost per step. Another advantage

of these is they do not generate new local maxima or minima (or total variation diminishing property in time) because of the time discretization. In the present work, we use five-stage fourth-order SSP-RK scheme [or SSP-RK (5,4)] for WENO5 and KL schemes. Note that the allowable time step for this scheme is greater than that of the Shu–Osher fourth-order scheme and fourth-order explicit RK scheme (Gottlieb et al. 2001). The CFL limit for this scheme is approximately 1.5. The SSP-RK (5,4) scheme can be written in the following way:

$$\overline{U}^{(0)} = \overline{U}^n,$$
$$\overline{U}^{(i)} = \sum_{k=0}^{(i-1)}[\alpha_{ik}\overline{U}^k + \Delta t\beta_{ik}L(\overline{U}^k)], \quad i = 1, 2, \dots, s,$$
$$\overline{U}^{n+1} = \overline{U}^{(s)}.$$

Constants α_{ik} and β_{ik} are given in appendix B.

b. Positivity-preserving filters

The WENO schemes can control spurious oscillations in the solution to a great extent, nevertheless, there is no guarantee that it will always keep the numerical solution within the legitimate (physical) bounds. The numerical solution with WENO schemes may still have small amplitude oscillations, in other words, these schemes are only "essentially" nonoscillatory, but not strictly positivity preserving. Another issue is that the final semidiscrete FV equation (8) itself may be a source for tiny spurious negative numbers due to numerical precision errors. This is because on the right side of (8), time tendencies are computed as differences of fluxes through the cell walls, when the values of the fluxes are very close, the net result may have a negative sign (with very small magnitude). For many atmospheric tracers such as humidity and mixing ratios, the global maximum and minimum values are known in advance, moreover, for which negative values are not acceptable. To address this issue we implement optional positivity-preserving filters to the CUFV schemes.

First, we discuss a bound-preserving (BP) conservative filter, which is particularly useful when the global minimum and maximum value of the solution is known in advance. In the present work we implement the BP filter for the schemes considered. The BP filter relies on local reconstruction polynomial, and it is computationally inexpensive. The BP filter is based on the Liu and Tadmor (1998) limiter. Recently, Zhang and Shu (2010) extended this for high-order discontinuous Galerkin (DG) schemes, and Zhang and Nair (2012) implemented the BP filter for a DG transport scheme on the cubed sphere. We apply this filter for both WENO5 and KL reconstruction polynomials.

Let $P_{ij}(x, y)$ be a reconstruction polynomial on a cell Ω_{ij} with a known cell average of $\overline{U}_{ij}$. The BP filter replaces $P_{ij}(x, y)$ by a bound preserving reconstruction $\tilde{P}_{ij}(x, y)$ as follows:

$$\tilde{P}_{ij}(x, y) = \theta_{ij} P_{ij}(x, y) + (1 - \theta_{ij})\overline{U}_{ij}, \qquad (13)$$

where the limiter function $\theta_{ij} \in [0, 1]$, is defined as

$$\theta_{ij} = \min\left\{ \left| \frac{M - \overline{U}_{ij}}{M_{ij} - \overline{U}_{ij}} \right|, \left| \frac{m - \overline{U}_{ij}}{m_{ij} - \overline{U}_{ij}} \right|, 1 \right\}, \qquad (14)$$

where M and m are the global maximum and minimum values, respectively, of the initial condition. The local extrema M_{ij}, m_{ij} on a cell Ω_{ij} are given by

$$M_{ij} = \max_{(x,y) \in \Omega_{ij}} \{P_{ij}(x, y)\}, \quad m_{ij} = \min_{(x,y) \in \Omega_{ij}} \{P_{ij}(x, y)\}. \qquad (15)$$

The extrema M_{ij} and m_{ij} are numerically evaluated from the reconstructed point values on the cell boundary, which are corrected using (13) and then $\tilde{P}_{ij}(x, y)$ can be used for computing fluxes.

A scheme is considered to be positive definite, if it does not introduce any negative values in the computed solution from nonnegative initial values. However, because of arithmetic precision errors as mentioned above, the solutions with very small magnitude might still have negative signs. A positivity-preserving (or sign preserving) (PP) filter may be applied at the final stage of computation to completely eliminate unacceptable negative solution. To ensure the positivity of the solution, we employ the PP filter based on an upstream renormalization approach developed by Smolarkiewicz (1989). For oscillations with small amplitude this filter is very robust, and we apply the PP filter as the finalization process for CUFV combined with BP filter. The PP filter is local, computationally cheap, and easy to implement. Recently, Blossey and Durran (2008) implemented the PP filter for their FV schemes, this is in fact, a special case of the flux-corrected transport (FCT) algorithm (Durran 1999). The details of the PP algorithm can be found in Smolarkiewicz (1989). Note that the BP filter is only applicable when the global extrema M and m are known, and it is considered to be a limitation of this approach (Zhang and Nair 2012).

4. Numerical experiments

For the spherical advection experiments, we use several benchmark tests such as the solid-body rotation tests and the deformational-flow tests. One can use the point values created at the cell centers with the (exact)

initial condition $U(t = 0)$, as the cell averages (Lauritzen et al. 2010). However, for better consistency, we create 3×3 point values initially on each cell (see Fig. 1c), and then the cell-averaged value $\overline{U}_{ij}$ is computed by the following Simpson's rule:

$$\begin{aligned} \overline{U}_{ij} = \frac{1}{36}(&U_{i-1/2,j-1/2} + U_{i-1/2,j+1/2} + U_{i+1/2,j-1/2} \\ &+ U_{i+1/2,j+1/2} + 4U_{i-1/2,j} + 4U_{i+1/2,j} \\ &+ 4U_{i,j-1/2} + 4U_{i,j+1/2} + 16U_{ij}). \end{aligned} \qquad (16)$$

The normalized standard errors ℓ_1, ℓ_2, and ℓ_∞ used for the test cases are as those defined in Nair and Lauritzen (2010).

a. Solid-body rotation tests

We first consider the solid-body rotation test proposed by Williamson et al. (1992), where a "cosine bell" is used as scalar field U. Since the exact solution is known at all times, error measures can be computed. The cosine bell is defined in spherical coordinates (λ, θ), where λ is the longitude and θ is the latitude:

$$U(\lambda, \theta, 0) = \begin{cases} (h_0/2)[1 + \cos(\pi r_d/r_0)] & \text{if} \quad r_d < r_0 \\ 0 & \text{if} \quad r_d \geq r_0, \end{cases} \qquad (17)$$

where r_d is the great-circle distance between (λ, θ) and the center of the bell. The cosine bell with base radius $r_0 = R_a/3$ is placed at $(\lambda_c, \theta_c) = (3\pi/2, 0)$, which corresponds to the center of the face (F_4) on the cube. The height of the bell is $h_0 = 1000$ m, and radius of the earth $R_a = 6.371\,22 \times 10^6$ m. The spherical velocity components (u_s, v_s) of the nondivergent wind field are defined to be

$$\begin{aligned} u_s &= u_0(\cos\alpha_0 \cos\theta + \sin\alpha_0 \cos\lambda \sin\theta) \quad \text{and} \\ v_s &= -u_0 \sin\alpha_0 \sin\lambda. \end{aligned}$$

Here $u_0 = (2\pi R_a)/(12\text{ days})$ and α_0 is the angle between axis of cosine-bell rotation and the polar axis of the spherical coordinate system. It takes 12 simulated days (288 h) to complete one revolution around the sphere. When $\alpha_0 = 0$, $\pi/2$, and $\pi/4$, the flow is oriented along the equator (east–west), poles (north–south), and diagonal (northeast) directions, respectively. The flow along the northeast direction is the most challenging case, since the bell passes through four vertices and two edges to complete one revolution around the sphere; we use this particular configuration.

Although the cosine-bell initial condition is widely used for testing the accuracy of spherical advection schemes, it is not a good choice for convergence study because the scalar field (17) is only a C^1 function. For convergence tests we consider a smooth Gaussian

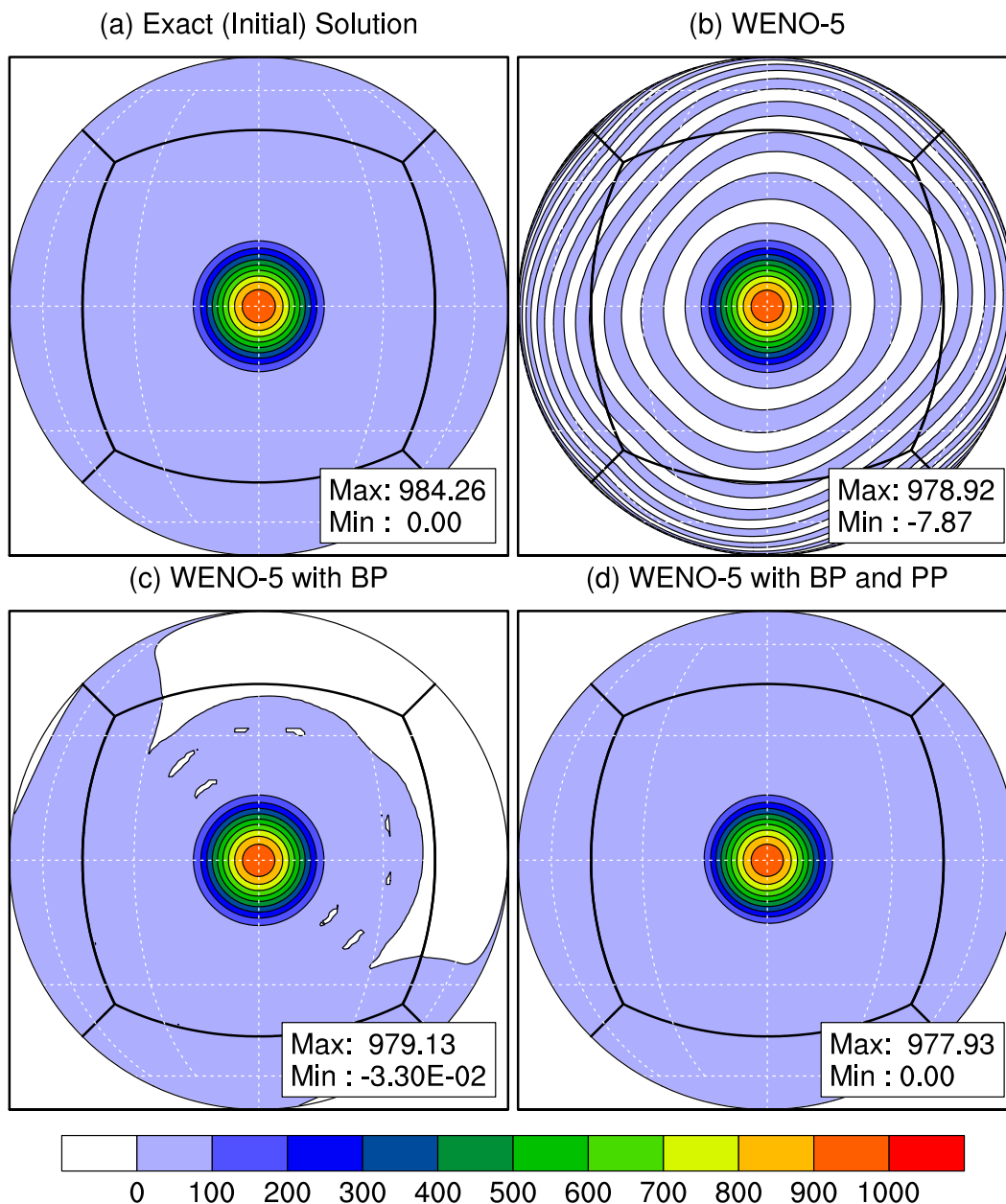## Demonstration of Filters: Cosine-Bell Advection Test

FIG. 4. Results of the cosine-bell advection test on the cubed sphere after one revolution (12 days) with the WENO5 scheme. The wind field is oriented along the northeast direction ($\alpha_0 = \pi/4$), on a $48 \times 48 \times 6$ grid ($N_c = 48$), with $C_{max} = 0.25$. (a) Initial (cell averaged) height (m) of the cosine bell, (b) numerical solution without any filter, (c) solution with BP filter, and (d) solution with the BP and PP filters.

distribution (C^∞), which is defined as below in terms of absolute Cartesian coordinates:

$$(X, Y, Z) = (R_a \cos\theta \cos\lambda, R_a \cos\theta \sin\lambda, R_a \sin\theta), \quad (18)$$

$$U(\lambda, \theta, 0) = h_{max} \exp\{-b_0[(X - X_c)^2 + (Y - Y_c)^2 + (Z - Z_c)^2]\}, \quad (19)$$

where the parameters $h_{max} = 1000\,\mathrm{m}$, $b_0 = 40\,\mathrm{m}^{-2}$ so that the Gaussian profile has a comparable *height* and base *radius* with that of the cosine bell on the sphere. The center of the Gaussian profile is initially located at $(\lambda_c, \theta_c) = (3\pi/2, 0)$, which corresponds to the Cartesian coordinates (X_c, Y_c, Z_c), and is related through (18). All other parameters including the wind field are set to be
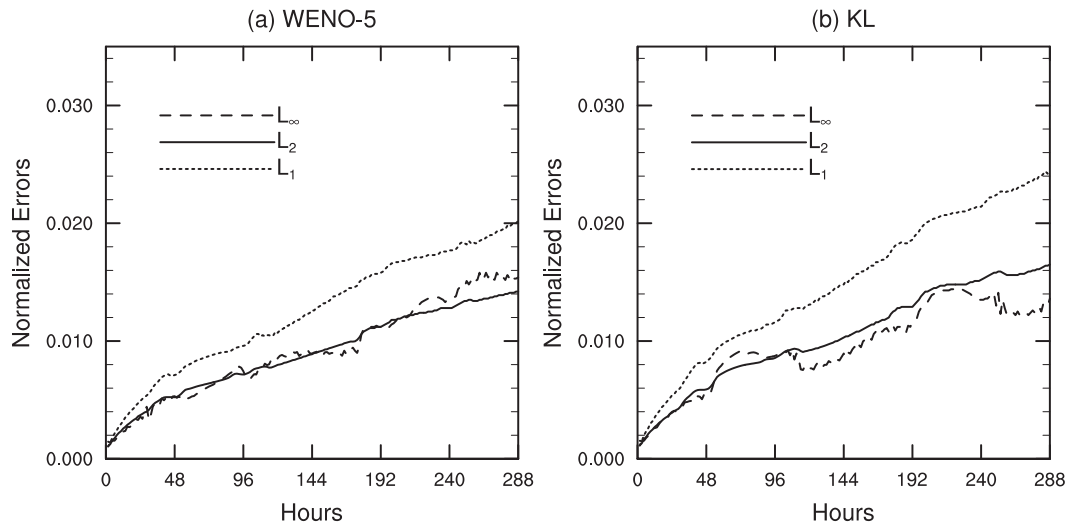
Normalized Errors: Solid-Body Rotation (Cosine-Bell)

FIG. 5. Time traces of the normalized errors ℓ_1, ℓ_2, and ℓ_∞ for the cosine-bell advection test with the (a) WENO5 and (b) KL schemes. Flow is along the northeast direction ($\alpha_0 = \pi/4$) on the cubed sphere at a resolution $40 \times 40 \times 6$, for 12 days ($N_{step} = 192$ for one revolution).

the same as in the case of cosine-bell test. For the solid-body rotation tests we report on the global maximum of the directional Courant numbers C_{max}, which is defined as follows (Rossmanith 2006):

$$C_{max} = \max\left(|u^1| \frac{\Delta t}{\Delta x^1}, |u^2| \frac{\Delta t}{\Delta x^2} \right), \qquad (20)$$

and the number of time steps $N_{step} = 12$ days/Δt, required for a complete revolution on the sphere.

First, we demonstrate the effect of BP and PP filters with the cosine-bell advection test. For this experiment the WENO5 scheme was selected on a $48 \times 48 \times 6$ (or $N_c = 48$) cubed-sphere grid with $\alpha_0 = \pi/4$, $N_{step} = 1350$, and $C_{max} \approx 0.25$. The solutions after one revolution are shown in Fig. 4 for different combinations of the filters. Without using any filter the WENO5 scheme produces spurious oscillations (see Fig. 4b, where the minimum value ≈ -8 m). Spurious oscillations in the solution are successfully suppressed by the BP filter. Nevertheless, there are still minute negative values [$\mathcal{O}(-10^{-3})$] left in the solution (Fig. 4c), which are completely removed by applying the PP filter, as seen in Fig. 4d. In addition, we have compared the time traces of normalized ℓ_2 errors for different combinations of the filters, however, the application of BP and PP filters did not degrade the accuracy of the scheme (results are not shown).

To compare the results with other high-order FV models, we conducted additional experiments for the cosine-bell test. At a resolution $40 \times 40 \times 6$ with $N_{step} = 192$ (i.e.,

$\Delta t = 90$ min, $C_{max} \approx 1.4$), the ℓ_1, ℓ_2, and ℓ_∞ errors for WENO5 (with the BP filter) are 0.0202, 0.0142, and 0.0153, respectively. Time tracers of normalized errors are shown in Fig. 5, where the results with WENO5 are slightly better than that with the KL scheme for ℓ_1 and ℓ_2 errors, but the ℓ_∞ error is smaller for the KL scheme. No obvious noises are generated by cubed-sphere edges and the interpolation seems to be performing as expected. Note that this experiment configuration is similar to that used by Ullrich et al. (2010) for a fourth-order FV scheme for their Fig. 5; however, error measures are smaller for both WENO5 and KL cases. This indicates that the interpolation procedure we used at the cubed-sphere edges is accurate. When the number of time steps is further decreased to $N_{step} = 160$ ($C_{max} \approx 1.7$), the error measures are $\ell_1 = 0.0242$, $\ell_2 = 0.0172$, and $\ell_\infty = 0.0131$; showing WENO5 is still accurate at a higher Courant number.

This experiment is repeated for a lower grid resolution $32 \times 32 \times 6$ with $N_{step} = 256$ ($C_{max} \approx 0.9$), and the normalized errors are $\ell_1 = 0.0401$, $\ell_2 = 0.0276$, and $\ell_\infty = 0.0245$. With the same experimental set up the conservative semi-Lagrangian multitracer transport scheme (CSLAM; Lauritzen et al. 2010), produces errors $\ell_1 = 0.0765$, $\ell_2 = 0.0414$, and $\ell_\infty = 0.0255$, higher than the results with WENO5. Note that CSLAM is a third-order conservative semi-Lagrangian method that does not require special interpolation procedure at the cubed-sphere edges, as required in the case of typical Eulerian FV methods. The fourth-order FV method

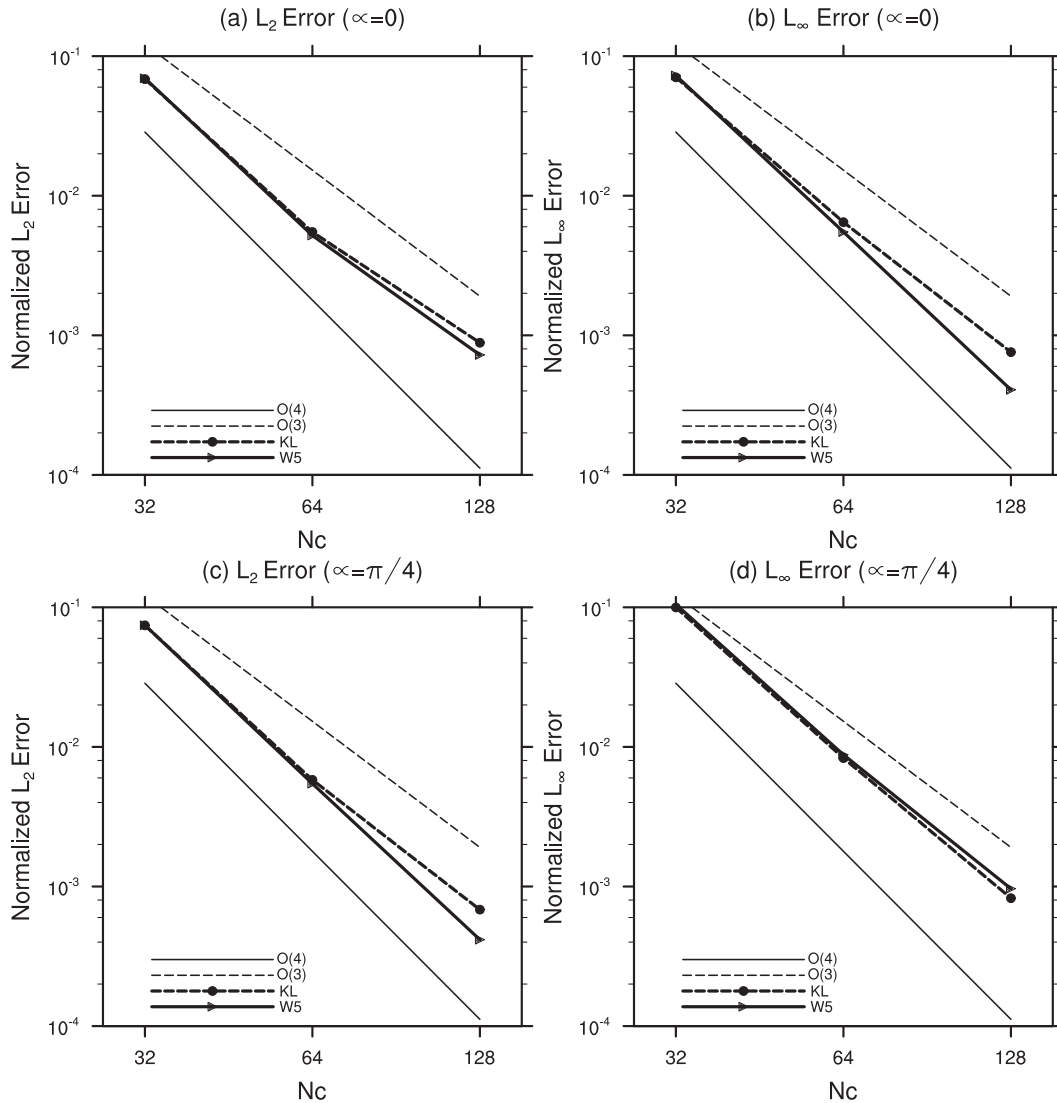## Gaussian Hill Advection (W5 vs. KL)

FIG. 6. Convergence results with the solid-body rotation of a Gaussian hill for the WENO5 and KL schemes. The normalized errors (a) ℓ_2 and (b) ℓ_∞, when the flow is along the equator ($\alpha_0 = 0$). The normalized errors (c) ℓ_2 and (d) ℓ_∞, when the flow is in the northeast direction ($\alpha_0 = \pi/4$).

(Chen and Xiao 2008) and the third-order discontinuous Galerkin method (Zhang and Nair 2012) are essentially based on multimoment approach. Although they are relatively expensive algorithms, they possess several computationally attractive features such as multiple degrees of freedom for each cell to evolve in time and compact computational stencils (no or smaller halo regions), because of that they have robust ways to handle flux exchanges at the cubed-sphere edges. This could be a reason why the error measures reported by these schemes for solid-body rotation test at a resolution $32 \times 32 \times 6$ are better than those results with WENO5 or KL scheme.

Figure 6 shows the convergence of normalized errors (ℓ_2, ℓ_∞) for the solid-body rotation test with a smooth Gaussian hill (19) initial condition. We achieved a third- to fourth-order convergence with both the WENO and KL scheme, for different flow orientations ($\alpha_0 = 0$, $\pi/4$), where the WENO5 scheme has a slightly better convergence rate as opposed to the KL scheme. The ℓ_∞ error (Figs. 6b,d) shows a better convergence rate for both schemes for equatorial flow ($\alpha_0 = 0$). For a solid-body rotation test with a Gaussian hill on 2D Cartesian grid, we observed fourth-order convergence rate (results are not shown) for both the WENO5 and KL schemes. We cannot expect the same order of accuracy on the cubed-sphere

Initial, Half and Final Fields: Moving-Vorticies Test

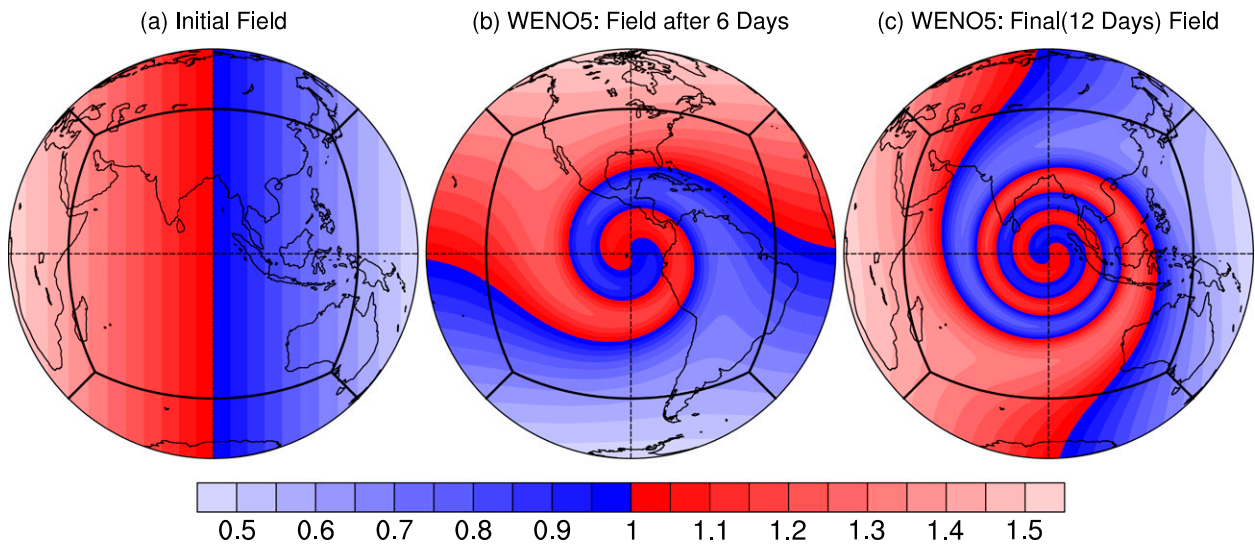| (a) Initial Field	(b) WENO5: Field after 6 Days	(c) WENO5: Final(12 Days) Field

FIG. 7. Numerical solution with the WENO5 scheme for the moving vortices test. (a) Initial vortex field, (b) solution at halftime (6 days), and (c) solution at after full evolution (12 days). The vortices move along the northeast direction ($\alpha_0 = \pi/4$) while evolving. A cubed sphere with $N_c = 80$ and $C_{\max} \approx 0.25$ is used for the simulation.

grid because of its inherent complexity. This indicates that a reason for degradation in convergence rate is mostly due to the corner-cell handling by quadratic interpolation and the ghost-cell approximation for the KL scheme.

b. Deformational flow test: Moving vortices

The first deformational test we use is the "moving vortices" test case introduced in Nair and Jablonowski (2008). Two steady vortices are created on a sphere, whose centers are located at diametrically opposite sides. The flow field is nondivergent, time dependent, and highly deformational; the vortices move along a great-circle trajectory while deforming, with the known exact solution. This test is more challenging than the solid-body rotation test, and particularly useful for advection schemes developed on cubed-sphere geometry. For the current tests, the vortex flow field is oriented along the northeast direction ($\alpha_0 = \pi/4$) so that the vortex centers pass through the vertex and edges of the cubed sphere. The exact solution at time t is defined by (Nair and Jablonowski 2008):

$$U(\lambda', \theta', t) = 1 - \tanh\left[\frac{\rho}{\gamma_0} \sin(\lambda' - \omega(\theta')t)\right],$$

where (λ', θ') are the rotated spherical coordinates with respect to the regular (λ, θ) coordinates, $\rho = \rho_0 \cos\theta'$ is the radial distance of the vortex, and the parameters $\rho_0 = 3$ and $\gamma_0 = 5$. Angular velocity $\omega(\theta')$ is defined in terms of tangential velocity V_t:

$$\omega(\theta') = \begin{cases} V_t/(R_a\rho) & \text{if} \quad \rho \neq 0, \\ 0 & \text{if} \quad \rho = 0, \end{cases}$$

and the tangential velocity of the vortex field is defined by

$$V_t = u_0 \frac{3\sqrt{3}}{2} \operatorname{sech}^2(\rho) \tanh(\rho),$$

where $u_0 = 2\pi R_a/(12\text{days})$, scaled such that 12 model days are required for the full evolution of the vortices, which is the same time taken for a complete revolution around the sphere. The time-dependent wind field (u_s, v_s) is given by

$$u_s(t) = u_0(\cos\theta \cos\alpha_0 + \sin\theta \cos\lambda \sin\alpha_0)$$
$$+ R_a\omega\{\sin\theta_c(t)\cos\theta - \cos\theta_c(t)\cos[\lambda - \lambda_c(t)]\sin\theta\},$$
$$v_s(t) = -u_0(\sin\lambda \sin\alpha_0) + R_a\omega\{\cos\theta_c(t)\sin[\lambda - \lambda_c(t)]\},$$

where α_0 is the flow orientation parameter as used in the solid-body rotation case. Initial conditions for the vortex field are $U(\lambda', \theta', 0)$, with a vortex center kept at $[\lambda_c, (t = 0), \theta_c(t = 0)] = (3\pi/2, 0)$.

The cubed-sphere resolution is chosen to be $80 \times 80 \times 6$ (or $N_c = 80$, which corresponds to $1.125°$ resolution at the equator) so that the results could be compared to that with CSLAM and FV (Putman and Lin 2007) schemes. The flow fields are oriented along the northeast direction ($\alpha_0 = \pi/4$) with $N_{\text{step}} = 750$. Figure 7 shows initial, halftime (6 days), and final (12 days) vortex fields in Figs. 7a, 7b, and 7c, respectively, where the numerical simulations (Figs. 7b and 7c) are done with
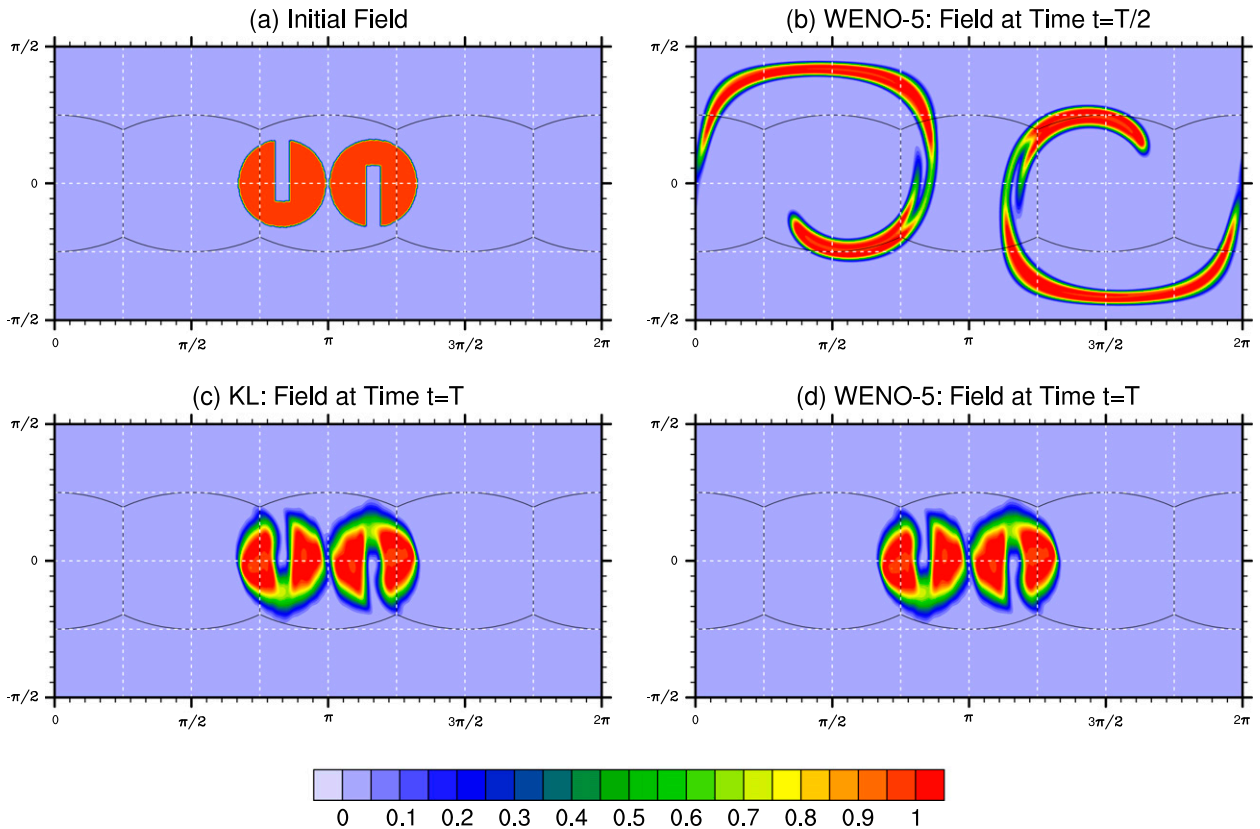
FIG. 8. Numerical solution for the deformational flow test on a cubed sphere with mesh $90 \times 90 \times 6$ with twin slotted cylinders as the initial condition. (a) The initial solution in which these two cylinders move along the zonal direction while deforming, and reach the initial position after making a complete revolution. The solution after time (b) $T/2$ and (d) $T = 5$ (nondimensional time units) using the WENO5 scheme, and (c) the solution after time T using the KL scheme.

the WENO5 scheme. For brevity we do not show the time series of normalized errors. After a complete revolution without BP filter, the normalized errors with the WENO5 scheme are $\ell_1 = 0.0021$, $\ell_2 = 0.0042$, and $\ell_\infty = 0.0191$, and with the KL scheme errors are $\ell_1 = 0.0021$, $\ell_2 = 0.0043$, and $\ell_\infty = 0.0194$. When the BP filter is applied, the WENO5 errors are $\ell_1 = 0.0024$, $\ell_2 = 0.0043$, and $\ell_\infty = 0.0190$ and the corresponding errors for the KL scheme are $\ell_1 = 0.0024$, $\ell_2 = 0.0042$, and $\ell_\infty = 0.0193$. Thus, application of the BP filter causes only a slight change for ℓ_1, ℓ_2, and ℓ_∞ errors. This is an important feature of the BP filter, which does not destroy the accuracy of smooth fields while keeping the solution bounded. However, a typical slope limiter (van Leer 1974; Colella and Woodward 1984) may clip the legitimate extrema of smooth solution. Note that qualitatively there is no significant difference between the solution with the WENO5 and KL schemes. The results with the moving vortex test case are comparable to the third-order CSLAM, and that reported by Putman and

Lin (2007), which is an FV scheme combined with high-order boundary treatment.

c. Deformational flow test: Slotted cylinders

To further validate the CUFV schemes on the sphere, we use a challenging benchmark deformational flow test case recently developed by Nair and Lauritzen (2010). We are particularly interested in nonsmooth (twin slotted cylinder) initial conditions. The initial distributions are deformed into thin filaments halfway through the simulation while they are being transported along the zonal direction by the solid-body component of the flow.

The initial twin slotted-cylinder data are given by

$$U(\lambda, \theta) = \begin{cases} c & \text{if} \quad r_i \leq r, |\lambda - \lambda_i| \geq r/6, i = 1, 2, \\ c & \text{if} \quad r_1 \leq r, |\lambda - \lambda_1| < r/6, \theta - \theta_1 < -5/12r, \\ c & \text{if} \quad r_2 \leq r, |\lambda - \lambda_2| < r/6, \theta - \theta_2 > 5/12r, \\ b & \text{otherwise}, \end{cases}$$
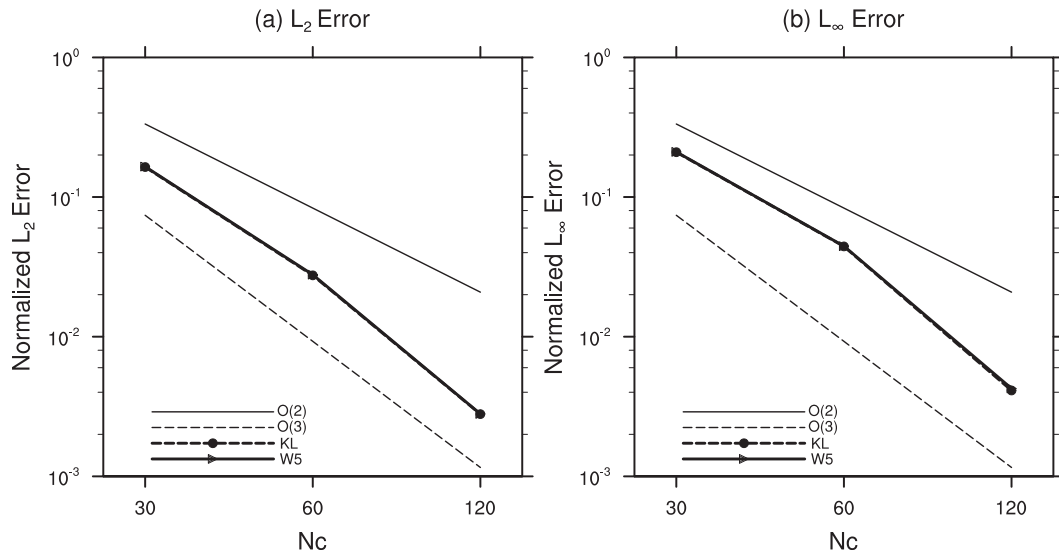
Deformational Flow: Gaussian Fields (W5 vs. KL)

FIG. 9. Convergence for the deformational flow with double-Gaussian fields for the normalized errors (a) ℓ_2 and (b) ℓ_∞ for the WENO5 and KL schemes.

where $c = 1$, $b = 0.1$, the radius of the cylinder $r = 1/2$, and $r_i = r_i(\lambda, \theta)$ is the great-circle distance between (λ, θ) and a specified center (λ_i, θ_i) of the unit sphere:

$$r_i(\lambda, \theta) = \arccos[\sin\theta_i \sin\theta + \cos\theta_i \cos\theta \cos(\lambda - \lambda_i)].$$

The initial positions of the centers of the distributions are at $(\lambda_1, \theta_1) = (5\pi/6, 0)$ and $(\lambda_2, \theta_2) = (7\pi/6, 0)$, respectively. The slots are oriented in opposite directions for the two cylinders so that they are symmetric with respect to the flow. Figure 8a shows the initial position.

The wind field is nondivergent but highly deformational. The initial distributions are deformed into thin filaments halfway through the simulation while they are being transported along the zonal direction by the solid-body component of the flow. Note that an exact solution for this test is only available at the final time $t = T$, and it is identical to the initial condition. The time-dependent nondivergent wind field is defined as

$$u_s(\lambda, \theta, t) = \kappa \sin^2(\lambda') \sin(2\theta) \cos(\pi t/T) + 2\pi \cos(\theta)/T$$
$$v_s(\lambda, \theta, t) = \kappa \sin(2\lambda') \cos(\theta) \cos(\pi t/T),$$

where $\lambda' = \lambda - 2\pi t/T$, $\kappa = 2.0$, and $T = 5$ in nondimensional time units.

The same test case can be used for convergence studies, if the slotted cylinders are replaced by two symmetrically located Gaussian hills in (19), as discussed in Nair and Lauritzen (2010). Recently, this test case has been considered in Lauritzen et al. (2012) for comparing various advection schemes. The initial smooth fields (C^∞) undergo extreme deformation and translation during the simulation, and return to their initial position at the final time step. This test is designed to be very challenging for global transport schemes especially on the cubed sphere. We consider this test to further evaluate the convergence of the WENO5 and KL schemes.

Figure 8 shows the results of the deformational flow tests with the WENO5 scheme in Figs. 8b and 8d, respectively, at halftime ($t = T/2$) and final time ($t = T$). Figure 8c shows the results with KL scheme at final time. The normalized errors at final-time T, with the WENO5 scheme are $\ell_1 = 0.146$, $\ell_2 = 0.175$, and $\ell_\infty = 0.533$, and with the KL scheme errors are $\ell_1 = 0.147$, $\ell_2 = 0.175$, and $\ell_\infty = 0.534$. The maximum initial CFL for this simulation was $C_{\max} \approx 0.75$, on a cubed-sphere grid with $N_c = 90$. The WENO5 and KL schemes results are comparable to those reported in Nair and Lauritzen (2010). It is clear from Fig. 8 that the BP and PP filters used in the schemes completely remove the spurious oscillations.

Figure 9 shows the convergence of the normalized errors with smooth deformational flow involving double-Gaussian fields. Clearly both WENO5 and KL show more than second-order convergence for the complex flow fields, and the results are comparable to

the CSLAM scheme as shown in Lauritzen et al. (2012). The semi-Lagrangian scheme with reduced dependence (flux based) on grid geometry shows a better convergence rate for this test as shown in Erath and Nair (2014). A degradation in the convergence may be due to the fact that both schemes rely on a quadratic interpolation method at the corner (halo) cells of the cubed sphere. A rigorous approach would be employing the compact Hermit interpolation recently introduced by Croisille (2013) or interpolation with localized radial basis functions at the cubed-sphere corners. However, we do not consider these advanced methods for the present study.

We roughly calculated the execution time taken by each scheme for the same test. From the comparison results we found that the WENO5 and KL schemes take almost same amount of time to compute. In general, our comparison study indicates that the dimension-by-dimension WENO5 is very competitive as compared to the fully two-dimensional KL scheme in terms of accuracy and efficiency.

5. Summary and conclusions

Central-upwind finite-volume (CUFV) schemes are a class of Godunov-type method for solving hyperbolic conservation laws, and combine the nice features of the classical upwind and central FV methods. Semidiscrete central schemes are high-order accurate and nonoscillatory, depending on the reconstruction procedure, and these features make them computationally attractive for atmospheric numerical modeling. We consider semidiscretized high-order CUFV schemes with a dimension-by-dimension fifth-order WENO reconstruction (WENO5) and a fourth-order fully 2D (KL) reconstruction. The flux computations are based on flux formula introduced in Kurganov and Petrova (2001), which employs a compact approach and relies on local wind speed. Time integration is performed with a fourth-order Runge–Kutta method for the WENO5 and KL schemes.

The WENO-based schemes are only *essentially* nonoscillatory indicating that oscillations of small amplitude will still remain in the solution. In a strict sense WENO schemes are not positivity preserving. To address the positivity issue, a bound-preserving (BP) conservative filter is combined with WENO reconstructions, and a positivity-preserving (PP) filter is used. The BP and PP filters are local and computationally inexpensive. To compare these schemes we use several benchmark tests on the cubed-sphere geometry. The cubed-sphere geometry is a challenging computational domain for FV schemes, because of the

nonorthogonal curvilinear geometry and grid discontinuities at the edges and corners. We used a 1D interpolation method to extend grid points (ghost cells) along the great-circle arc at the edges for computational stencils. This interpolation procedure combines quadratic and cubic-Lagrange interpolations and does not require a third panel at the corner ghost cell, which simplifies the implementation of the WENO5 and KL schemes.

The advection tests on the sphere include solid-body rotation of a cosine bell and moving (deforming) vortices. These two tests are quasi smooth; all the error norms show that the results with WENO5 and KL schemes are very close. In addition, a new challenging deformational flow test was also used to assess the performance of the nonoscillatory scheme in the presence of strong discontinuities. The BP and PP filter combination perform very well for the nonsmooth problem, and it does not degrade the accuracy when the problem is smooth. The execution time was roughly calculated using the WENO5 scheme as a basic reference, and it shows that KL scheme takes little less time to compute and produces similar results. The error norms suggest that the results with spherical WENO5 and KL are comparable to those published with recent high-order (global) FV schemes (Ullrich et al. 2010; Chen and Xiao 2008).

The 1D component of the WENO5 scheme is fifth-order accurate, nevertheless, the dimension-by-dimension approach may cause reduction in the formal order of accuracy of the resulting 2D scheme to second order. However, the empirical convergence rate for a smooth solid-body rotation test indicates that both the WENO5 and KL schemes maintain an order of accuracy between the third and fourth order. For a very challenging deformational flow test (Lauritzen et al. 2012) the order of accuracy further reduces, and is in between the second and third order. Unfortunately other high-order FV models (recently published) do not report empirical convergence results with the deformational flow tests.

In terms of practical implementation (algorithmic simplicity), WENO5 is a clear winner because the underlying computational stencil is simple and does not require corner ghost cells. The 1D method used for creating halo regions may not be the best choice, especially for high-order fully 2D FV schemes. However, a new method based on a Hermitian compact stencil is available (Croisille 2013) for cubed-sphere grids for high-order interpolations. We will further investigate this approach for our future applications. The Gaussian quadrature approach proposed by Ullrich et al. (2010) might be a good option for the 2D KL scheme, and is a

topic for a future study. The benefits of BP and PP filters with CUFV schemes will be further studied for preservation of the tracer correlation and other desirable properties required for atmospheric chemistry applications (Lauritzen et al. 2012). It is not clear whether the WENO5 can perform better than a fully 2D scheme for nonlinear problems. This will be a matter for a future study, using a nonlinear global shallow-water model. Work in this direction is progressing and will be reported elsewhere.

APPENDIX A

2D KL Scheme Reconstruction Details

To evaluate the flux $H_{i\pm1/2,j}$, $H_{i,j\pm1/2}$ in (8), eight point values along the cell walls (as indicated in Fig. 2) are required. The reconstructed point values at eight points on a single cell (i.e., {E, W, N, S, SE, SW, NE, NW}) can be obtained by the following:

$$U_{ij}^{E} = C_1 + C_2 + C_4 + C_9 + C_{12},$$
$$U_{ij}^{W} = C_1 - C_2 + C_4 - C_9 + C_{12},$$
$$U_{ij}^{S} = C_1 + C_3 + C_5 + C_{10} + C_{13},$$
$$U_{ij}^{N} = C_1 - C_3 + C_5 - C_{10} + C_{13},$$
$$U_{ij}^{NE} = U_{ij}^{E} + C_3 + C_5 + C_6 + C_7 + C_8 + C_{10} + C_{11} + C_{13},$$
$$U_{ij}^{SE} = U_{ij}^{E} - C_3 + C_5 - C_6 - C_7 + C_8 - C_{10} + C_{11} + C_{13},$$
$$U_{ij}^{NW} = U_{ij}^{W} + C_3 + C_5 - C_6 + C_7 - C_8 + C_{10} + C_{11} + C_{13},$$
$$U_{ij}^{NE} = U_{ij}^{W} - C_3 + C_5 + C_6 + C_7 - C_8 - C_{10} + C_{11} + C_{13}.$$

$$(A1)$$

The details of the auxiliary quantities C_i are given as follows:

$$C_1 = (7084\overline{U}_{ij} - 368\sigma_1^{xy}\overline{U}_{ij} + 27\sigma_1^{xy}\overline{U}_{ij} + 10\sigma_d\overline{U}_{ij})/5760,$$
$$C_2 = (36D_1^x\overline{U}_{ij} - 5D_2^x\overline{U}_{ij} - D_1^x\overline{U}_{ij+1} - D_1^x\overline{U}_{ij-1})/96,$$
$$C_3 = (36D_1^y\overline{U}_{ij} - 5D_2^y\overline{U}_{ij} - D_1^y\overline{U}_{i+1j} - D_1^y\overline{U}_{i-1j})/96,$$
$$C_4 = (38\sigma_1^x\overline{U}_{ij} - 3\sigma_2^x\overline{U}_{ij} + 2\sigma_1^y\overline{U}_{ij} - \sigma_D\overline{U}_{ij} - 70\overline{U}_{ij})/192,$$
$$C_5 = (38\sigma_1^y\overline{U}_{ij} - 3\sigma_2^y\overline{U}_{ij} + 2\sigma_1^x\overline{U}_{ij} - \sigma_D\overline{U}_{ij} - 70\overline{U}_{ij})/192,$$
$$C_6 = (D_1^x\overline{U}_{ij+1} - D_1^x\overline{U}_{ij-1})/16,$$
$$C_7 = (D_1^y\overline{U}_{i+1j} - D_1^y\overline{U}_{i-1j} - 2D_1^x\overline{U}_{ij})/32,$$
$$C_8 = (D_1^x\overline{U}_{ij+1} - D_1^x\overline{U}_{ij-1} - 2D_1^y\overline{U}_{ij})/32,$$
$$C_9 = (D_2^x\overline{U}_{ij} - 2D_1^x\overline{U}_{ij})/96,$$
$$C_{10} = (D_2^y\overline{U}_{ij} - 2D_1^y\overline{U}_{ij})/96,$$
$$C_{11} = (4\overline{U}_{ij} - 2\sigma_1^{xy}\overline{U}_{ij} + \sigma_d\overline{U}_{ij})/64,$$
$$C_{12} = (6\overline{U}_{ij} - 4\sigma_1^x\overline{U}_{ij} + \sigma_2^x\overline{U}_{ij})/384,$$
$$C_{13} = (6\overline{U}_{ij} - 4\sigma_1^y\overline{U}_{ij} + \sigma_2^y\overline{U}_{ij})/384.$$

The discrete operators are given as

$$\sigma_1^x\overline{U}_{ij} = \overline{U}_{i-1j} + \overline{U}_{i+1j}, \quad \sigma_2^x\overline{U}_{ij} = \overline{U}_{i-2j} + \overline{U}_{i+2j},$$
$$\sigma_1^y\overline{U}_{ij} = \overline{U}_{ij-1} + \overline{U}_{ij+1}, \quad \sigma_2^y\overline{U}_{ij} = \overline{U}_{ij-2} + \overline{U}_{ij+2},$$
$$\sigma_1^{xy}\overline{U}_{ij} = \sigma_1^x\overline{U}_{ij} + \sigma_1^y\overline{U}_{ij}, \quad \sigma_2^{xy}\overline{U}_{ij} = \sigma_2^x\overline{U}_{ij} + \sigma_2^y\overline{U}_{ij},$$
$$D_1^x\overline{U}_{ij} = \overline{U}_{i+1j} - \overline{U}_{i-1j}, \quad D_2^x\overline{U}_{ij} = \overline{U}_{i+2j} - \overline{U}_{i-2j},$$
$$D_1^y\overline{U}_{ij} = \overline{U}_{ij+1} - \overline{U}_{ij-1}, \quad D_2^y\overline{U}_{ij} = \overline{U}_{ij+2} - \overline{U}_{ij-2},$$
$$\sigma_d\overline{U}_{ij} = \overline{U}_{i-1j-1} + \overline{U}_{i+1j+1} + \overline{U}_{i+1j-1} + \overline{U}_{i-1j+1}.$$

APPENDIX B

Constants for the SSP-RK(5,4) Scheme

The following are the values of the constants required by the SSP-RK(5,4) scheme:

$\alpha_{10} = 1.0$ $\alpha_{20} = 0.444\,370\,494\,067\,34$

$\alpha_{21} = 0.555\,629\,505\,932\,66$ $\alpha_{30} = 0.620\,101\,851\,385\,40$

$\alpha_{32} = 0.379\,898\,148\,614\,60$ $\alpha_{40} = 0.178\,079\,954\,107\,73$

$\alpha_{43} = 0.821\,920\,045\,892\,27$ $\alpha_{50} = 0.006\,833\,258\,840\,39$

$\alpha_{52} = 0.517\,231\,672\,089\,78$ $\alpha_{53} = 0.127\,598\,311\,332\,88$

$\alpha_{54} = 0.348\,336\,757\,736\,94$ $\beta_{10} = 0.391\,752\,227\,003\,92$

$\beta_{21} = 0.368\,410\,592\,629\,59$ $\beta_{32} = 0.251\,891\,774\,247\,38$

$\beta_{43} = 0.544\,974\,750\,212\,37$ $\beta_{53} = 0.084\,604\,163\,382\,12$

$\beta_{54} = 0.226\,007\,483\,193\,95$ $\alpha_{31,41,42,51} = 0.0$

$\beta_{20,30,31,40,41,42,50,51,52} = 0.0.$

REFERENCES

Adamy, K., B. Bousquet, S. Faure, J. Lammie, and R. Temam, 2010: A multilevel method for finite volume discretization of the two-dimensional nonlinear shallow-water equations. *Ocean Modell., 33,* 235–256, doi:10.1016/j.ocemod.2010.02.006.

Blossey, P. N., and D. R. Durran, 2008: Selective monotonicity preservation in scalar advection. *J. Comput. Phys., 227,* 5160–5183, doi:10.1016/j.jcp.2008.01.043.

Byron, S., and D. Levy, 2006: On the total variation of high-order semi-discrete central schemes for conservation laws. *J. Sci. Comput., 27,* 163–175, doi:10.1007/s10915-005-9046-8.

Chen, C., and F. Xiao, 2008: Shallow water model on cubed-sphere by multi-moment finite volume method. *J. Comput. Phys., 227,* 5019–5044, doi:10.1016/j.jcp.2008.01.033.

Cheruvu, V., R. D. Nair, and H. M. Tufo, 2007: A spectral finite volume transport scheme on the cubed-sphere. *Appl. Numer. Math., 57,* 1021–1032, doi:10.1016/j.apnum.2006.09.008.

Colella, P., and P. R. Woodward, 1984: The Piecewise Parabolic Method (PPM) for gas-dynamical simulations. *J. Comput. Phys., 54,* 174–201, doi:10.1016/0021-9991(84)90143-8.

Croisille, J.-P., 2013: Hermitian compact interpolation on the cubed-sphere grid. *J. Sci. Comput., 57,* 193–212, doi:10.1007/s10915-013-9702-3.

Durran, D. R., 1999: *Numerical Methods for Wave Equations in Geophysical Fluid Dynamics.* Springer-Verlag, 465 pp.

Erath, C., and R. D. Nair, 2014: A conservative multi-tracer transport scheme for spectral-element spherical grids. *J. Comput. Phys., 256,* 118–134, doi:10.1016/j.jcp.2013.08.050.

Godunov, K. O., 1959: A difference scheme for numerical solution of discontinuous solution of hydrodynamic equations. *Math. Sbornik, 47,* 271–306.

Gottlieb, S., C.-W. Shu, and E. Tadmor, 2001: Strong stability-preserving high-order time discretization methods. *SIAM Rev., 43,* 89–112, doi:10.1137/S003614450036757X.

Kurganov, A., and D. Levy, 2000: A third-order semidiscrete central scheme for conservation laws and convection-diffusion equations. *SIAM J. Sci. Comput., 22,* 1461–1468, doi:10.1137/S1064827599360236.

——, and G. Petrova, 2001: A third-order semi-discrete genuinely multidimensional central scheme for hyperbolic conservation laws and related problems. *Numer. Math., 88,* 683–729, doi:10.1007/PL00005455.

——, and Y. Liu, 2012: New adaptive artificial viscosity method for hyperbolic systems of conservation laws. *J. Comput. Phys., 231,* 8114–8134, doi:10.1016/j.jcp.2012.07.040.

Lauritzen, P. H., R. D. Nair, and P. A. Ullrich, 2010: A conservative semi-Lagrangian multi-tracer transport scheme (CSLAM) on the cubed-sphere grid. *J. Comput. Phys., 229,* 1401–1424, doi:10.1016/j.jcp.2009.10.036.

——, W. Skamarock, M. Prather, and M. Taylor, 2012: A standard test case suite for two-dimensional linear transport on the sphere. *Geosci. Model Dev., 5,* 887–901, doi:10.5194/gmd-5-887-2012.

Levy, M. N., R. D. Nair, and H. M. Tufo, 2007: High-order Galerkin method for scalable global atmopsheric models. *Comput. Geosci., 33,* 1022–1035, doi:10.1016/j.cageo.2006.12.004.

Liu, X., and E. Tadmor, 1998: Third order non-oscillatory central scheme for hyperbolic conservation laws. *Numer. Math., 79,* 397–425, doi:10.1007/s002110050345.

——, S. Osher, and T. Chen, 1994: Weighted essentially non-oscillatory schemes. *J. Comput. Phys., 115,* 200–212, doi:10.1006/jcph.1994.1187.

Nair, R. D., and C. Jablonowski, 2008: Moving vortices on the sphere: A test case for horizontal advection problems. *Mon. Wea. Rev., 136,* 699–711, doi:10.1175/2007MWR2105.1.

——, and P. H. Lauritzen, 2010: A class of deformational flow test cases for linear transport problems on the sphere. *J. Comput. Phys., 229,* 8868–8887, doi:10.1016/j.jcp.2010.08.014.

——, and K. K. Katta, 2013: The central-upwind finite-volume method for atmospheric numerical modeling. *Recent Advances in Scientific Computing and Applications,* J. Li, H. Yang, and E. Machorro, Eds., American Mathematical Society, 277–286.

——, S. Thomas, and R. Loft, 2005: A discontinuous Galerkin transport scheme on the cubed sphere. *Mon. Wea. Rev., 133,* 814–828, doi:10.1175/MWR2890.1.

Norman, M. R., R. D. Nair, and F. H. M. Semazzi, 2011: A low communication and large time step explicit finite-volume solver for non-hydrostatic atmospheric dynamics. *J. Comput. Phys., 230,* 1567–1584, doi:10.1016/j.jcp.2010.11.022.

Putman, W. M., and S.-J. Lin, 2007: Finite-volume transport on various cubed-sphere grids. *J. Comput. Phys., 227,* 55–78, doi:10.1016/j.jcp.2007.07.022.

Rančić, M., R. J. Purser, and F. Mesinger, 1996: A global shallow water model using an expanded spherical cube. *Quart. J. Roy. Meteor. Soc., 122,* 959–982, doi:10.1002/qj.49712253209.

Ronchi, C., R. Iacono, and P. S. Paolucci, 1996: The cubed sphere: A new method for the solution of partial differential equations in spherical geometry. *J. Comput. Phys., 124,* 93–114, doi:10.1006/jcph.1996.0047.

Rossmanith, J. A., 2006: A wave propagation method for hyperbolic systems on the sphere. *J. Comput. Phys., 213,* 629–658, doi:10.1016/j.jcp.2005.08.027.

Sadourny, R., 1972: Conservative finite-difference approximations of the primitive equations on quasi-uniform spherical grids. *Mon. Wea. Rev., 100,* 136–144, doi:10.1175/1520-0493(1972)100<0136:CFAOTP>2.3.CO;2.

Shu, C.-W., 1997: Essentially non-oscillatory and weighed essentially non-oscillatory schemes for hyperbolic conservation laws. *Advanced Numerical Approximation of Nonlinear Hyperbolic Equations,* A. Quarteroni, Ed., Vol. 1697, *Lecture Notes in Mathematics,* Springer, 325–432, doi:10.1007/BFb0096355.

Smolarkiewicz, P., 1989: Comments on "A positive definite advection scheme obtained by nonlinear renormalization of the advective fluxes." *Mon. Wea. Rev., 117,* 2626–2632, doi:10.1175/1520-0493(1989)117<2626:COPDAS>2.0.CO;2.

Spiteri, R. J., and S. J. Ruuth, 2002: A new class of optimal high-order strong-stability-preserving time discretization methods. *SIAM J. Numer. Anal., 40,* 469–491, doi:10.1137/S0036142901389025.

Toro, E. F., 1999: *Riemann Solvers and Numerical Methods for Fluid Dynamics: A Practical Introduction.* 2nd ed. Springer-Verlag, 18 pp.

Ullrich, P. A., C. Jablonowski, and B. van Leer, 2010: High-order finite-volume methods for the shallow-water equations on the sphere. *J. Comput. Phys., 229,* 6104–6134, doi:10.1016/j.jcp.2010.04.044.

van Leer, B., 1974: Towards the ultimate conservative difference scheme. II. Monotonicity and conservation combined in a second-order scheme. *J. Comput. Phys., 14,* 361–370, doi:10.1016/0021-9991(74)90019-9.

Williamson, D. L., J. B. Drake, J. J. Hack, R. Jakob, and P. N. Swarztrauber, 1992: A standard test set for numerical approximations to the shallow water equations in spherical

geometry. *J. Comput. Phys.,* **102,** 211–224, doi:10.1016/S0021-9991(05)80016-6.

Yang, C., and X. Cai, 2011: Parallel multilevel methods for implicit solution of shallow water equations with nonsmooth topography on the cubed-sphere. *J. Comput. Phys.,* **230,** 2523–2539, doi:10.1016/j.jcp.2010.12.027.

——, J. Cao, and X. Cai, 2010: A fully implicit domain decomposition algorithm for shallow water equations on the cubed-sphere. *SIAM J. Sci. Comput.,* **32,** 418–438, doi:10.1137/080727348.

Zhang, X., and C.-W. Shu, 2010: On maximum-principle-satisfying high order schemes for scalar conservation laws. *J. Comput. Phys.,* **229,** 3091–3120, doi:10.1016/j.jcp.2009.12.030.

Zhang, Y., and R. D. Nair, 2012: A nonoscillatory discontinuous Galerkin transport scheme on the cubed sphere. *Mon. Wea. Rev.,* **140,** 3106–3126, doi:10.1175/MWR-D-11-00287.1.